Fine-Motion Planning in the Contact Space of Narrow-Clearance Assemblies [1]

Gordon Dakin [2] Robin Popplestone

CS Technical Report 93-60

July 9, 1993

Laboratory for Perceptual Robotics
Department of Computer Science
A265, Graduate Research Center
University of Massachusetts
Amherst, MA 01003

Abstract

A fine-motion planning technique is described for assemblies with narrow insertion clearances. A fine-motion planner receives as input a nominal assembly motion plan, computed from kinematic constraints alone. As described in a companion paper [4], the planner constructs an adjacency graph for each local contact space surrounding a problematic configuration in the nominal trajectory. A heuristic search of the adjacency graph produces a sequence of contact states that can be traversed in the presence of pose uncertainty, thus maneuvering the assembly past the problematic configuration. The rapid synthesis of a fine-motion trajectory through the selected contact states is facilitated by the nearly hyperpolyhedral nature of local contact space. The trajectory's distance to contact space facets representing undesired contact state transitions is maximized, and the resulting fine-motion plan is expressed as a sequence of hybrid control strategy specifications. Fine-motion trajectories produced by this technique have been successfully executed by a Zebra-0 robot.

---

[1] With the exception of section 4 and related appendices, this paper appeared in the *Proceedings of the 1993 IASTED International Conference on Robotics and Manufacturing*, pp. 206-8.

[2] Preparation of this paper was supported by grants IRI-9208920 and CDA-8922572 from the National Science Foundation.

1 Introduction

In many assembly tasks, particularly those involving small clearances, the set of feasible motions is centered around a single, nominal trajectory which arises naturally from the geometries of parts [11][14]. Due to the limited rotational freedom permitted by the narrow clearances, the local contact spaces surrounding points along the nominal trajectory are nearly hyperpolyhedral, providing simplified motion-planning domains in which to construct piecewise-linear trajectories.

In our "two-phase" approach to fine-motion planning, a nominal trajectory is supplied *a priori* by a high-level planner such as *KA3* [11], which derives trajectory configurations from geometric constraints alone, disregarding the effects of uncertainty. The *critical points* are then identified in the nominal trajectory, consisting of the problematic configurations where jamming and collisions are likely to arise in the presence of uncertainty. Assuming the insertion clearances are narrow, as is usually the case in industrial assembly, each critical point configuration is surrounded by a local, 6-dimensional contact space whose locally "flat" surfaces are well approximated by affine spaces. As described in the companion paper [4], an adjacency graph of contact states is constructed for each local contact space to support the planning of contact state transitions and fine-motion trajectories.

The present paper focuses on the planning of fine motions within a local contact space. Fine-motion planning proceeds at two hierarchical levels: at the higher level, a heuristic search of the adjacency graph of contact states yields a traversable sequence of contact states, whose traversal may be viewed as carefully maneuvering the assembly past the critical point in question without sticking or jamming. Restricting the assembly to a single, predetermined sequence of contact states mitigates the complexity of path planning. At the lower level of planning, a piecewise-linear trajectory is generated within the nearly hyperpolyhedral domain of the chosen contact states. The output of the fine-motion planner consists of a sequence of hybrid control strategy specifications for traversing each selected state.

In the two-phase approach to fine-motion planning, uncertainty issues are considered only after the initial creation of a nominal trajectory. This approach contrasts with the *LMT methods* [8][12], which synthesize multistep, nominal trajectories in a "single phase", through the recursive backchaining of subgoal regions. Unfortunately, the double-exponential complexity of the

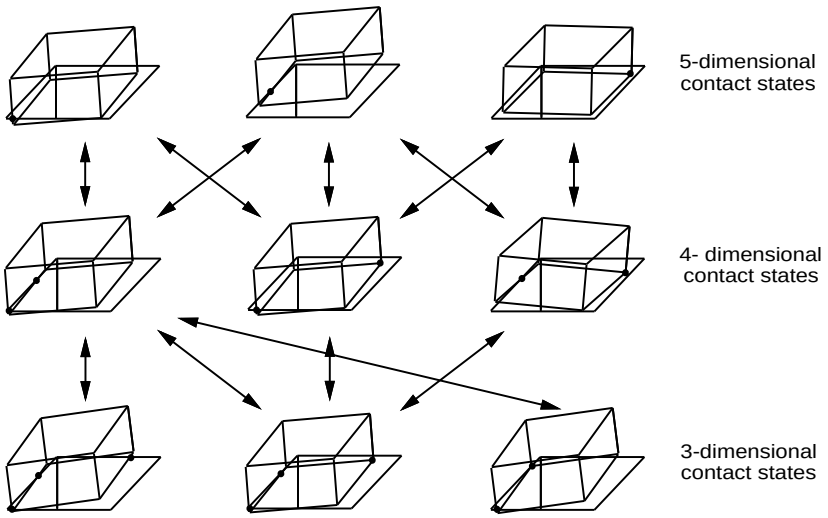

Figure 1. Adjacency graph of contact states.

LMT approach [3] has prevented its implementation outside of very restrictive domains. Our fine-motion planning technique differs from two phase methods based on *corrective compliance* [13][15][16], where a control strategy is derived to correct deviations of the moving part from the nominal trajectory. The present approach *replaces* the nominal trajectory with fine motions planned within the local contact spaces surrounding the critical points in the original trajectory. Our restriction of the assembly motion to a determinate sequence of contact states is also characteristic of the *manual* methods [2][16], whose selection of a single sequence of contact states facilitates the manual derivation of command trajectories, applied forces, and compliances. Whereas our technique relies on heuristics to select an appropriate sequence of contact states within a graph representation of contact space, Donald [7], Laugier [10], and the authors [6] previously employed heuristics at the lower planning level of trajectory formation. Finally, our iterative refinement of the command trajectory resembles the *flexible trajectory* techniques of gross motion planning [1], in which the trajectory's clearance with respect to environmental obstacles is iteratively optimized.

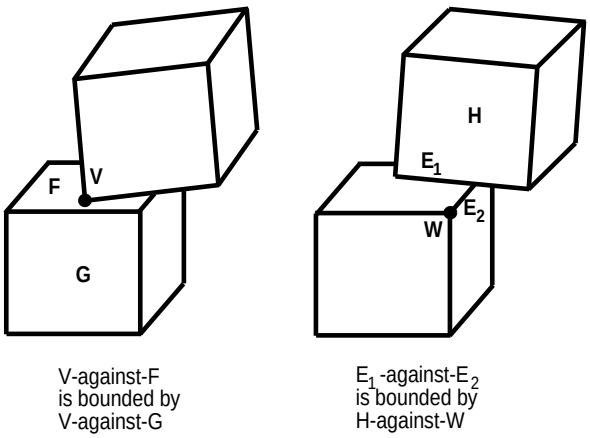

Figure 2. Primitive contact bounds.

2 Representing contact space

To support the heuristic search for a traversable sequence of contact states within a local contact space, the multidimensional facets of the contact space are enumerated and represented in an adjacency graph of contact states. A portion of the contact state adjacency graph for the first critical point configuration of the square peg-in-hole assembly is shown in figure 1. The analysis and construction of local contact spaces is described in detail in the companion paper [4] and reviewed here briefly.

Within each local contact space, the moving part's pose is characterized as a perturbation vector $\mathbf{X}$ in $\Re^6$, comprised of a translational $\mathbf{dx} = [dx\, dy\, dz]^T$ and a rotation $\delta\mathbf{x} = [\delta x\, \delta y\, \delta z]^T$. The local 6-dimensional C-space surrounding a critical point is bounded by 5-dimensional C-surfaces, which correspond to the *primitive contacts* (PCs) that can occur near the critical point. For polyhedral objects, each PC is a single-point contact involving either a convex vertex and a face, or two convex edges. The C-surface of primitive contact PC_i is characterized by a function $f_i : \Re^6 \rightarrow \Re$. A moving part pose $\mathbf{X}$ lies on the C-surface of PC_i if $f_i(\mathbf{X}) = 0$. The poses for which $f_i(\mathbf{X}) < 0$ lie on the side of the *forbidden zone*, wherein the assembly parts overlap. The derivation of a PC function f_i, and a formula for a PC's hyperplanar tangent surface, are found in [4] and Appendix I, respectively.

The 5-dimensional contact space facet associated with a PC may have bor-

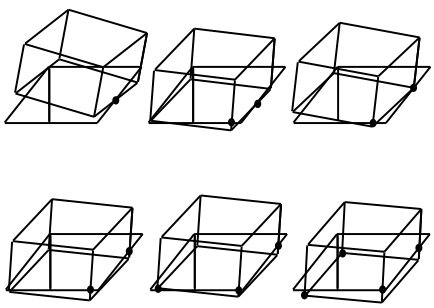

Figure 3. A C-state sequence.

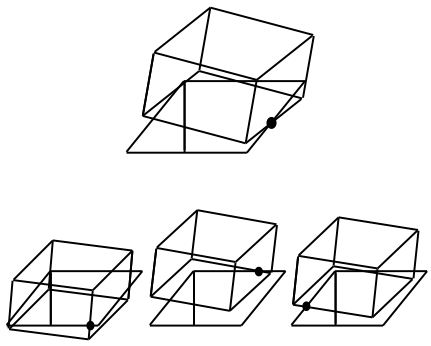

Figure 4. Obstacle PCs.

ders corresponding to the finite extent of the assembly part's surface features. In figure 2, the contact involving vertex V and face F is bounded by the convex edge shared by F and its adjacent face G. The poses $\mathbf{X} \in \Re^6$ associated with the PC formed by V and F are confined to the halfspace $g(\mathbf{X}) < 0$, where g is just the C-surface function for V-against-G.

The point set S_i in $\Re^6$ associated with a primitive contact PC_i consists of the portion of the contact's C-surface that lies behind its bounding PCs' C-surfaces but not in the forbidden zone. When computing the distance between a command trajectory segment and an "obstacle" PC (see section 3), it is preferable to represent the PC as a convex set. PC_i's point set S_i is generally concave, however, owing to the concavity of the forbidden zone. Ignoring the presence of the forbidden zone, PC_i and its n_i bounding contacts PC_{ij} define a convex point set

$$S_i' = \{\mathbf{X} \mid f_i(\mathbf{X}) = 0,\ f_{ij}(\mathbf{X}) < 0,\ j = 1 \ldots n_i\} \tag{1}$$

When calculating the distance between a trajectory segment and the point set S' of an obstacle PC, the PC's closest point may actually lie in the forbidden zone of a closer, intervening obstacle PC. Since we are typically concerned with the distance to the *closest* obstacle PC, however, the correctness of more distant PCs' proximities is relatively unimportant.

3 Planning a fine-motion path

Fine-motion planning in local contact space takes place at two hierarchical levels: the higher-level selection of an appropriate sequence of contact states, and the lower-level formation of a piecewise-linear command trajectory through the chosen contact states. At the higher level, a heuristic search of a contact state adjacency graph (see figure 1) yields a traversable sequence of contact states. The sequence begins at a designated start state, such as free space, and ends at a suitable goal state, such as a 1- or 2-dimensional contact state shared by the local contact space surrounding the next critical point. Figure 3 shows a contact state sequence for the square peg-in-hole assembly.

In best-first search of the contact state adjacency graph, the relative merits of alternative trajectories are embodied in a cost function, combining (1) the number of contact state transitions, (2) the difficulty in distinguishing the force signatures of the chosen contact states from likely "error states" outside of the sequence, and (3) the danger that the assembly will deviate from the selected path and encounter an obstacle PC (see figure 4). The latter criterion depends on the quality of the command trajectory formed within the chosen contact states.

The fine-motion trajectory is defined by the sequential placement of goal poses within the selected contact states. Each contact state associated with the formation of a new contact is assigned an arbitrary goal pose $\mathbf{G}$, which together with its predecessor $\mathbf{S}$, defines a linear trajectory segment $\mathbf{L}$ (see figure 5). The goal pose $\mathbf{G}$ is then iteratively modified to increase the trajectory segment's clearance with respect to the obstacle PCs adjacent to the traversed state. The obstacle PCs are just the constituent PCs of the traversed state's adjacent, lower-dimensional "son" states, minus the PCs of the start and goal states.

The trajectory segment's proximity to each obstacle PC influences the estimated likelihood that the desired contact state transition will fail, as embodied in the following cost function:

$$cost(\mathbf{T}) \;=\; \sum \frac{1}{C - dist(\mathbf{L}, S_i')} \tag{2}$$

where proximity function $dist(\mathbf{L}, S_i')$ becomes negative when the trajectory segment overlaps the obstacle PC, and asymtote C is the overlap distance at which the cost becomes infinite. Note that the closest obstacles are the most

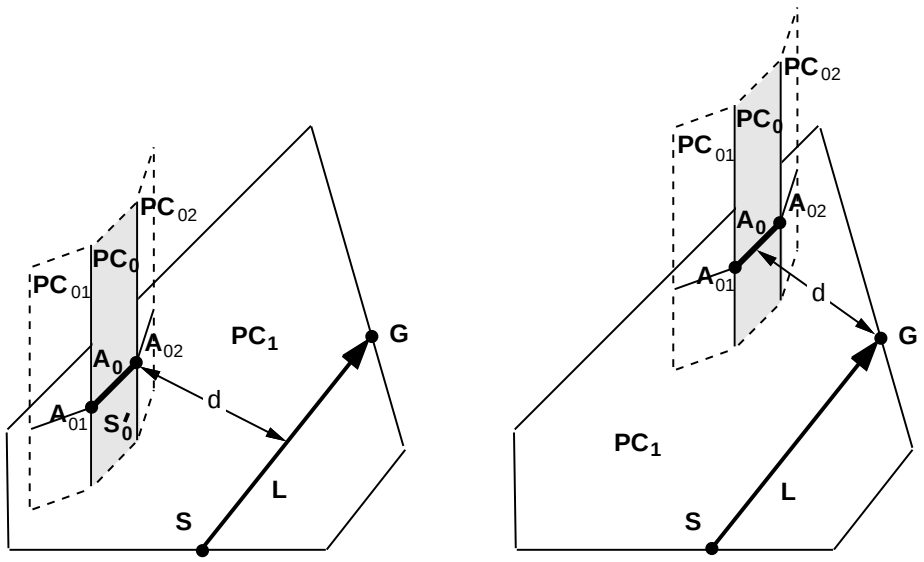

Figure 5. Measuring a trajectory's distance to obstacle PCs.

significant. The method of steepest descent is employed to perturb the goal pose along the goal state's surface until a minimum is encountered.

In its simplest form, the trajectory refinement procedure requires that an known ratio σ_r relates the expected degree of rotational uncertainty to translational uncertainty. To treat translational and rotational distance measurements equitably, a linear transformation $T : \Re^6 \rightarrow \Re^6$ is applied to contact space, "stretching" its rotational component by a factor of σ_r. As described in Appendix II, the descriptors $\mathbf{N}_i, D_i$ of each PC_i hyperplane are modified and represented in the scaled contact space. The distance calculations described below are then performed in the scaled contact space, where a unit of translational clearance with respect to an obstacle represents the same margin of safety as a unit of rotational clearance. A more precise treatment of uncertainty is presented in section 4, in which pose uncertainty is characterized by hyperellipsoids and their forward-projections in contact space.

The distance from a trajectory segment to an obstacle contact PC_0 is com-

puted as the shortest distance from PC_0's point set S_0' to the trajectory components **L**, **S**, and **G**. As figure 5 shows schematically in 3 dimensions, S_0' has one 5-dimensional (shaded) facet associated with PC_0 itself and two bordering 4-dimensional facets arising from its bounding contacts PC_A and PC_B. Since the uncertain trajectory is confined to the traversed state's C-surface, the relevant obstacles are in fact the (darkened) portions of these facets that intersect the traversed contact state.

Procedures for obtaining affine space approximations A_0, A_{0A}, A_{0B} for these facets are described in Appendix III, where a function *ASpace* computes the affine space of a contact state by intersecting its constituent PCs' affine spaces. The affine spaces for the obstacle facets in figure 5 are thus obtained:

$$\begin{aligned} A_0 &= ASpace_{\mathbf{G}}(PC_0, PC_1) \\ A_{0A} &= ASpace_{\mathbf{G}}(PC_0, PC_A, PC_1) \\ A_{0B} &= ASpace_{\mathbf{G}}(PC_0, PC_B, PC_1) \end{aligned} \tag{3}$$

The distance from an obstacle facet's affine space to trajectory component **L**, **S**, or **G** may be computed as described in Appendix IV, which presents a general procedure for calculating the closest points, and the separating distance, between two affine spaces. Referring once again to figure 5, the closest obstacle facet to **L**'s interior is A_{0A} or A_{0B}, provided the measurement extends to a point on **L** between **S** and **G**. The closest obstacle facet to **G** is A_0, provided the measurement extends to a point on A_0 between A_{0A} and A_{0B}. Otherwise, the closest facet is A_{0A} or A_{0B}.

3.1 Hybrid control strategy specification

Once a command trajectory has been synthesized in local contact space, each segment of the trajectory is expressed as a hybrid control strategy specification. Every specification includes (1) a set of position-controlled axes, i.e., a basis for the traversed state's affine space, (2) a complementary set of force-controlled axes, (3) the unit velocity of the moving part frame, as determined by the start and goal point of the trajectory segment, and (4) the termination condition for the control strategy. The traversed state's affine space is just $A = ASpace_{\mathbf{G}}(PC_1 \ldots PC_n)$, where $PC_1 \ldots PC_n$ are the PCs of the traversed state. A basis for A's complementary vector space provides the set of force-controlled axes. At a minimum, the termination condition is just the anticipated contact wrench, which is derived from the contact geometry of the newly established PC.

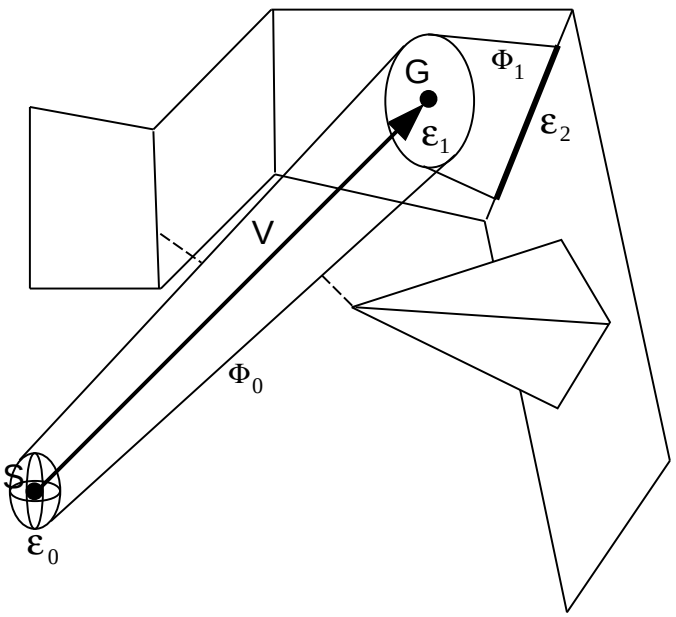

Figure 6. Forward-projections of ellipsoidal uncertainty regions.

4 Fine-motion planning with uncertainty

In this section, the trajectory refinement process is augmented with a more explicit analysis of uncertainty. Pose uncertainty is characterized as a hyperellipsoid ϵ (hereafter called an "ellipsoid") surrounding each succeessive command pose in the fine-motion trajectory (see figure 6). In the presence of velocity uncertainty, an uncertainty ellipsoid sweeps out a conic, forward-projection volume Φ. The trajectory refinement process is modified here to maximize the clearance of Φ, rather than the trajectory segment, with respect to obstacle PCs. Forward-projections are mentioned by authors of the LMT approach [8][10], who rely instead on back-projections and pre-images. Backpropagation is more suitable for planning which allows a nondeterministic sequence of contact states. Since the contact space facets to be traversed are known prior to uncertainty analysis in our approach, there is little to be gained from backpropagation. As demonstrated in the following sections, the construction of forward-projections based on ellipsoidal uncertainty models is both topologically simple and computationally inexpensive.

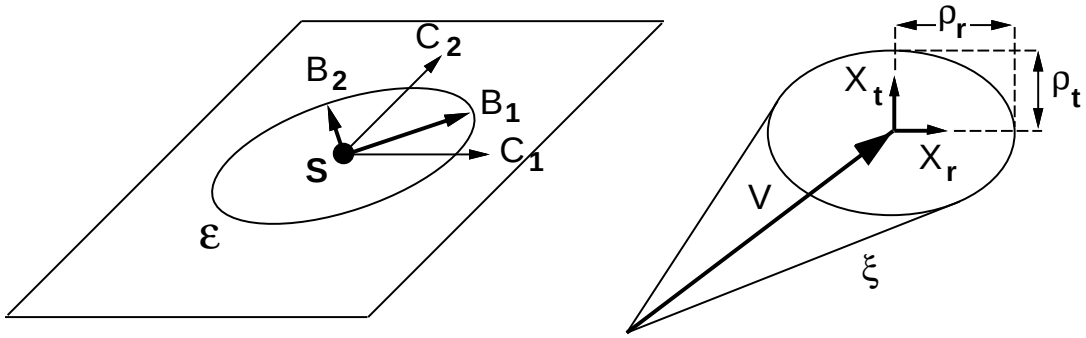

Figure 7. Uncertainty ellipse and velocity cone.

4.1 Representing uncertainty

The uncertainty region surrounding a trajectory point **S** is characterized as an ellipsoidal point set residing in the affine space of the trajectory point's contact state. The point set is bounded by an ellipsoid centered at **S**, with a surface equation expressed in a coordinate frame whose axes $\mathbf{C}_1 \ldots \mathbf{C}_n$ form a basis for the contact state's vector space. The surface equation $\mathbf{X}^T A \mathbf{X} = 1$ expresses the n-dinensional ellipsoid in the coordinate frame of the contact state. The symmetric, $n \times n$ matrix A may be diagonalized (or expressed *a priori* as a diagonal matrix):

$$A = BDB^T \tag{4}$$

where the columns of B are the principle axes of the ellipsoid (the eigenvectors of A), and diagonal matrix D holds the corresponding eigenvalues. Each eigenvalue $D_{ii} = 1/r_i^2$, where r_i is the radius corresponding to the ith principle axis. In figure 7, for example, an uncertainty ellipse ϵ lies in the affine space of a 2-dimensional contact state, with basis vectors $\mathbf{C}_1$ and $\mathbf{C}_2$. Centered at trajectory point **S**, the ellipse has two principle axes $\mathbf{B}_1, \mathbf{B}_2$, which are defined in $\mathbf{C}_1, \mathbf{C}_2$-space.

Velocity uncertainty is characterized as a velocity cone ξ whose ellipsoidal base bounds the maximum lateral displacement along any direction **U** perpendicular to the unit command velocity **V**. As shown in figure 7, the rate of increase in the uncertainty along translational axes $\mathbf{X}_t$ is assumed to be

a constant ρ_t, while the rate of increase along rotational axes $\mathbf{X}_r$ is denoted ρ_r. The rate of increase in uncertainty along a general perpendicular $\mathbf{U} \perp \mathbf{V}$ is provided as a function $\nu(\mathbf{U}, \mathbf{V})$, which returns the maximum displacement along $\mathbf{U}$ per unit command displacement along $\mathbf{V}$. The ellipsoidal bases for the velocity cones of all unit command velocities in C-space are represented *en masse* as a single, 6-dimensional ellipsoid:

$$\frac{1}{\rho_t^2}X_1^2 + \frac{1}{\rho_t^2}X_2^2 + \frac{1}{\rho_t^2}X_3^2 + \frac{1}{\rho_r^2}X_4^2 + \frac{1}{\rho_r^2}X_5^2 + \frac{1}{\rho_r^2}X_6^2 \;=\; 1 \tag{5}$$

The velocity cone base for a given command velocity $\mathbf{V}$ is the 5-dimensional ellipsoid where the ellipsoid (5) intersects the 5-dimensional vector space orthogonal to $\mathbf{V}$. For a general lateral displacement direction $\mathbf{U} \perp \mathbf{V}$, the rate of uncertainty is calculated by determining the point on the ellipsoid of equation (5) corresponding to direction $\mathbf{U}$. From Appendix V, the point in question is $\lambda_{\mathbf{u}}\mathbf{U}$, where

$$\lambda_{\mathbf{u}} \;=\; \frac{1}{\sqrt{\frac{u_1^2}{\rho_t^2} + \frac{u_2^2}{\rho_t^2} + \frac{u_3^2}{\rho_t^2} + \frac{u_4^2}{\rho_r^2} + \frac{u_5^2}{\rho_r^2} + \frac{u_6^2}{\rho_r^2}}} \tag{6}$$

Finally, we assume that a unit of rotational velocity gives rise to σ_r times the (translational and rotational) uncertainty arising from a unit of translational uncertainty. Accordingly, the command velocity is "stretched" along the rotational dimensions of C-space by a factor of σ_r, yielding a vector $\mathbf{V}'$ whose length reflects the degree of uncertainty associated with $\mathbf{V}$:

$$\mathbf{V}' \;=\; \begin{pmatrix} V_1 \\ V_2 \\ V_3 \\ \sigma_r V_4 \\ \sigma_r V_5 \\ \sigma_r V_6 \end{pmatrix} \tag{7}$$

In sum, the rate of increase in uncertainty along $\mathbf{U}$ associated with a command velocity is estimated to be

$$\nu(\mathbf{U}, \mathbf{V}) \;=\; \lambda_{\mathbf{U}} \, |\mathbf{V}'| \tag{8}$$

where $\lambda_{\mathbf{U}}$ and $\mathbf{V}'$ are calculated as in equations (6) and (7).

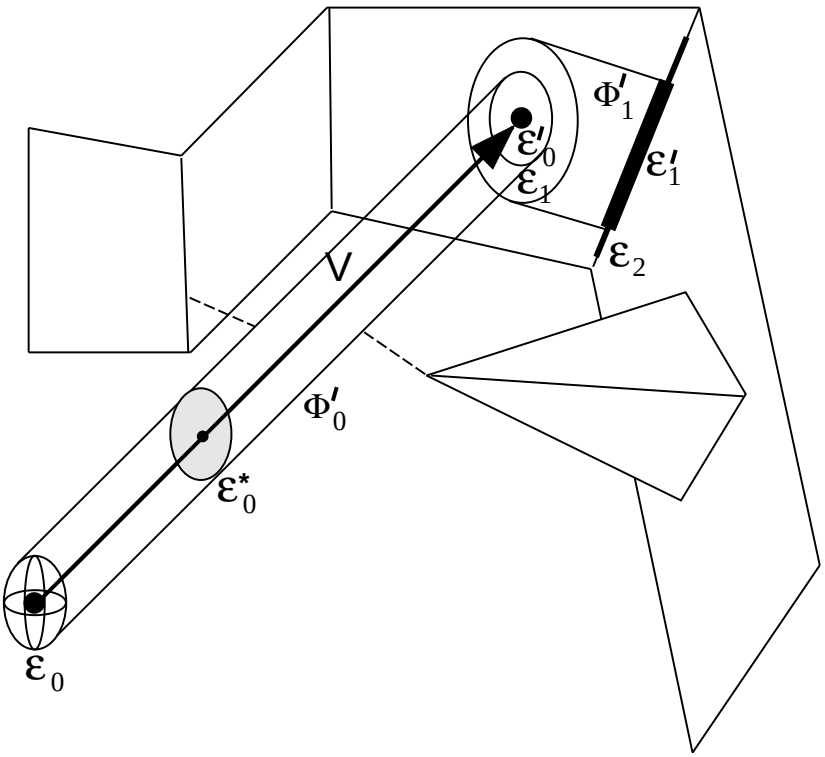

Figure 8. Cylindrical approximations of conic projections.

4.2 Computing forward-projection cross-sections

Assuming the velocity cone angle is small, a conic forward-projection may be approximated by a cylindrical volume whose ellipsoidal radii remain the same throughout the trajectory segment. As shown in figure 8, an uncertainty volume ϵ_0 sweeps out a cylindrical forward-projection Φ'_0, which approximates the expanding Φ_0 in figure 6. The uniformity of Φ'_0 along the command velocity, as well as lateral uniformity achieved through scaling in section 4.3, simplifies the task of measuring the forward-projection's proximity to obstacles. As seen in figure 8, the lateral expansion due to velocity uncertainty is nevertheless acknowledged when recovering the dimensions of the ellipsoid projection ϵ_1.

The cylindrical approximation of a forward-projection is represented by its

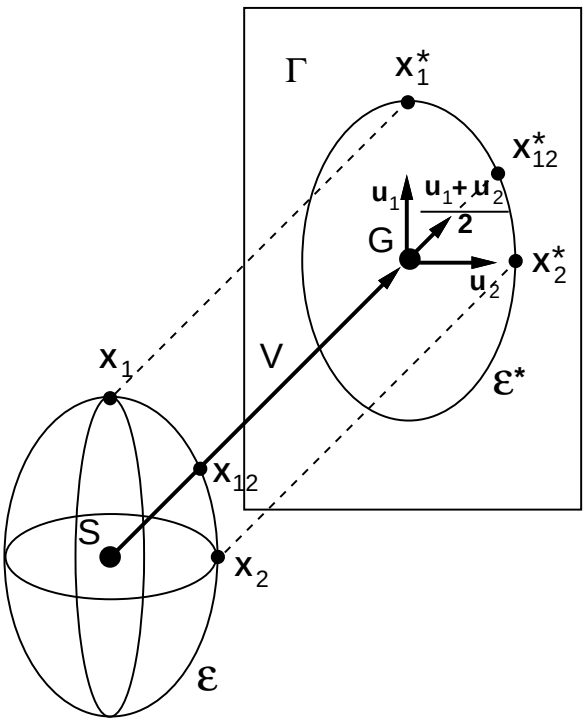

Figure 9. Computing the cross-section of a forward-projection.

cross-section ϵ^*, which sweeps out the cylindrical volume Φ' along the command velocity. The cylindrical volume Φ'_0 in figure 8, for example, is swept out by cross section ϵ^*_0 (not to be confused with ϵ_0's nonperpendicular projection ϵ'_0 onto the goal state). An ellipsoidal cross-section ϵ^* is computed as follows. We consider the case of an $(n+1)$-dimensional ellipsoid ϵ projected through an $(n+1)$-dimensional contact state, along command velocity $\mathbf{V}$. As shown in figure 9, the cross-section is obtained by projecting the ellipsoid onto an affine space Γ which is perpendicular to the command velocity. Γ is defined by the goal point $\mathbf{G}$ and a basis $\mathbf{U}_1 \ldots \mathbf{U}_n$ for the subspace of the traversed state's vector space which is orthogonal to $\mathbf{V}$. The projection onto Γ is accomplished by projecting surface points of ϵ onto Γ and recovering the ellipse determined by the projected points. Defined in $\mathbf{U}_1 \ldots \mathbf{U}_n$-space, the projected points $\mathbf{X}^*_i$ are expressed as displacements relative to the goal point, which serves as ϵ^*'s

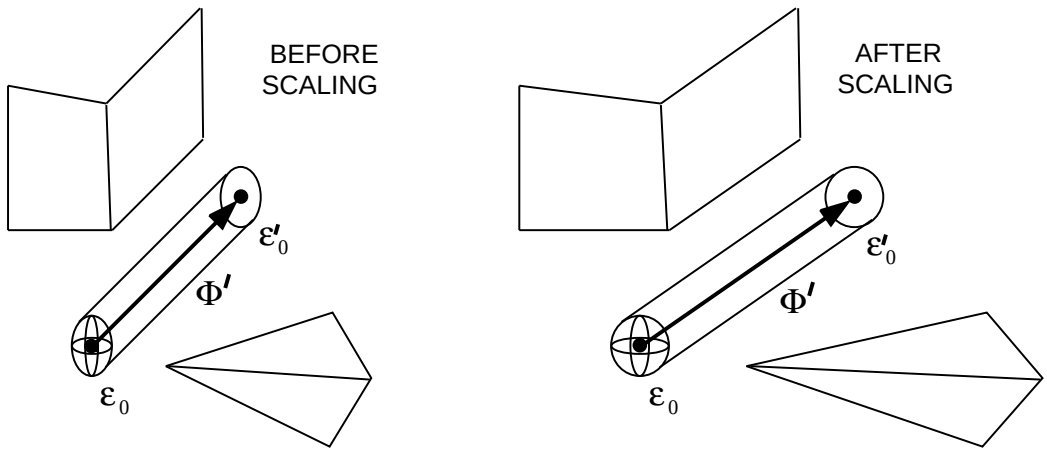

Figure 10. Scaling contact space to obtain uniform ellipsoid dimensions.

centroid. Recovery of ϵ''s surface equation $\mathbf{X}^T A^* \mathbf{X} = 1$ will require $n+\binom{n}{2}$ coefficients in its symmetric descriptor matrix A^*, so we project surface points corresponding to lateral directions $\mathbf{U}_1, \ldots, \mathbf{U}_n, (\mathbf{U}_i + \mathbf{U}_j)/2,\ (i,j \in 1 \ldots n, i \neq j)$. In the example of figure 9, where $n = 2$, the directions are just $\mathbf{U}_1$, $\mathbf{U}_2$, and $(\mathbf{U}_1 + \mathbf{U}_1)/2$. The surface points $\mathbf{X}_1, \mathbf{X}_2, \mathbf{X}_{12}$, of ϵ corresponding to these three directions may be computed as shown in Appendix V. The projected points $\mathbf{X}^*_1, \mathbf{X}^*_2, \mathbf{X}^*_{12}$, parameterize three equations in the three projected ellipsoid coefficients:

$$\begin{aligned} \mathbf{X}^{*T}_1 A^* \mathbf{X}^*_1 &= 1 \\ \mathbf{X}^{*T}_2 A^* \mathbf{X}^*_2 &= 1 \\ \mathbf{X}^{*T}_{12} A^* \mathbf{X}^*_{12} &= 1 \end{aligned} \tag{9}$$

In general n-space, the solution of $n+\binom{n}{2}$ equations in as many unknowns yields the coefficients in an $n \times n$ matrix A^*. Finally, A^* is diagonalized to obtain the principle axes $\mathbf{B}^*_i$ and corresponding radii (expressed as eigenvalues $1/r^{*2}_i$) of the ellipsoidal cross-section defined in $\mathbf{U}_1 \ldots \mathbf{U}_n$-space: $A^* = B^* D^* B^{*T}$. As required in section 4.3, we define a $6 \times n$ matrix C^* whose columns hold $\mathbf{U}_1 \ldots \mathbf{U}_n$, so that points defined in $\mathbf{U}_1 \ldots \mathbf{U}_n$-space, such as $\mathbf{X}$ satisfying ellipsoid equation $\mathbf{X}^T A^* \mathbf{X} = 1$, may be transformed to global point $C^* \mathbf{X} \in \Re^6$.

4.3 Trajectory refinement

Trajectory refinement with ellipsoidal uncertainty regions proceeds as described in section 3, except that the forward-projection's clearance, instead of the trajectory's, is iteratively maximized. To facilitate the distance measurements, a linear transformation $T' : \Re^6 \rightarrow \Re^6$ is applied to contact space to make the ellipsoidal cross-section ϵ^* of the cylindrical forward projection Φ' spherical (see figure 10). To achieve uniformity of ϵ^*'s radii $r_1 \ldots r_n$, we stretch contact space along each of ϵ^*'s major axes, making the scaled radii match the largest radius r_i. Specifically, contact space is scaled along the jth major axis by a factor of r_i/r_j, for $j = 1 \ldots n$. Since each major axis $\mathbf{B}_j^*$ is defined in $\mathbf{U}_1 \ldots \mathbf{U}_n$-space, it must first be transformed to the global frame. Contact space may be scaled along the global axes $C^* B_j^*$ by the scaling factor r_i/r_j, as described in Appendix II. Once the forward-projection's cross-section is uniformly spherical with radius r_i, its distance to an obstacle PC is just $d - r_i$, where d is the trajectory segment's distance to the obstacle PC (see section 3). For distance measurements to the goal point $\mathbf{G}$, the proximity vector $\mathbf{W}$ is generally nonperpendicular to the velocity $\mathbf{V}$, so the the measurement is modified as $d - r_i/(1 - \mathbf{V} \cdot \mathbf{W})$.

4.4 Recovering successive uncertainty ellipsoids

The uncertainty ellipsoid surrounding each trajectory point must be projected onto the affine space of the subsequent contact state, where it will, in turn, influence the refinement of the subsequent trajectory segment. As shown in figure 11, however, a conic forward-projection onto an affine space A yields a projected region whose centroid $\mathbf{G}'$ does not coincide with the projected image $\mathbf{G}$ of the cone's apex $\mathbf{S}$. In order to retain the goal point $\mathbf{G}$ of a trajectory as the centroid of the projected region and avoid a more complicated recovery of uncertainty ellipsoids, we approximate the ellipsoidal projection as follows. The procedure used in section 4.2 to compute a cylindrical forward-projection's cross-section is now modified to project the cross-section onto the affine space of the goal state. After recovering the resulting ellipsoid, the radii along its principle axes are increased to represent the lateral expansion arising from velocity uncertainty.

As in section 4.2, we consider the projection of an $(n + 1)$-dimensional ellipsoid ϵ through an $(n + 1)$-dimensional contact state. As illustrated in figure 12, for example, an ellipsoid ϵ_0 surrounding the starting point $\mathbf{S}$ of a

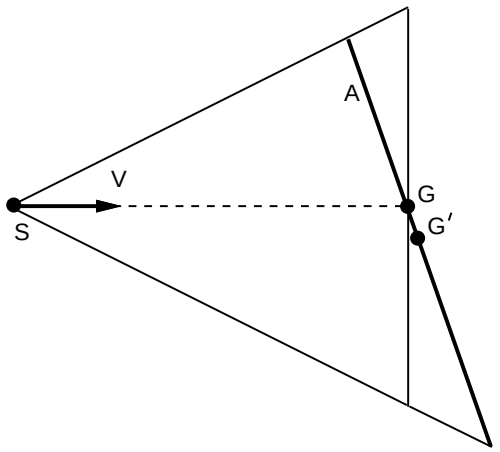

Figure 11. Migration of a conic projection's centroid.

trajectory segment is projected onto the affine space of the next contact state in the trajectory, yielding an ellipsoid ϵ_0'. The affine space of the goal state is defined by the goal point $\mathbf{G}$ and a vector space whose basis is contained in the columns of a $6 \times n$ matrix C'. The same surface points $\mathbf{X}_1, \mathbf{X}_2, \mathbf{X}_{12}$, of ϵ are projected as in section 4.2. Their projections $\mathbf{X}_1', \mathbf{X}_2', \mathbf{X}_{12}'$ are expressed in C''s column-space as displacements relative to the goal point. The projected points parameterize three equations in the three coefficients of the ellipse ϵ_0':

$$\begin{aligned} \mathbf{X}_1'^{\,T} A' \mathbf{X}_1' &= 1 \\ \mathbf{X}_2'^{\,T} A' \mathbf{X}_2' &= 1 \\ \mathbf{X}_{12}'^{\,T} A' \mathbf{X}_{12}' &= 1 \end{aligned} \tag{10}$$

The diagonalization of $A' = B'D'B'^T$ yields principle axes $\mathbf{B}_1'$ and $\mathbf{B}_2'$, whose radii are extracted from eigenvalues $1/r_1'^2$ and $1/r_2'^2$. As in section 4.2, this procedure generalizes to the case of an n-dimensional goal state, where $n + \binom{n}{2}$ goal projected points are required to determine the $n + \binom{n}{2}$ coefficients of symmetric matrix A'.

Finally, as shown in figure 12, the effects of velocity uncertainty are represented by enlarging the projected uncertainty region along its major axes. The lateral deviation vector $\mathbf{U}_i' \perp \mathbf{V}$ corresponding to major axis $\mathbf{B}_i$ is obtained as

$$\mathbf{U}_i' \;=\; C\,\mathbf{B}_i' \;-\; (C\,\mathbf{B}_i' \cdot \mathbf{V})\;\mathbf{V} \tag{11}$$

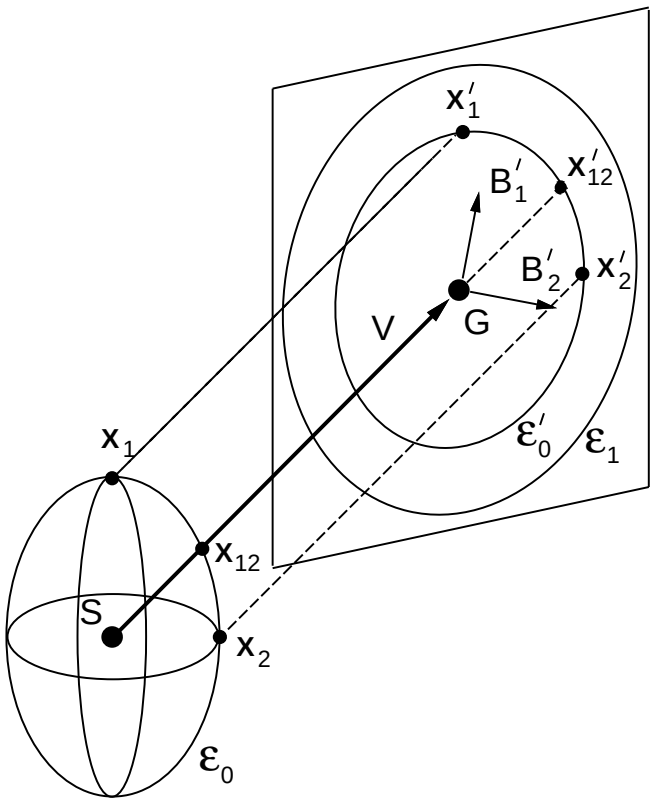

Figure 12. Recovering the projected uncertainty region.

and the velocity cone expands laterally along $\mathbf{U}_i'$ at a rate of $\nu(\mathbf{U}_i', \mathbf{V})$. The total lateral expansion along $\mathbf{U}_i'$ throughout the trajectory segment is therefore

$$v_i \;=\; \nu(\mathbf{U}_i', \mathbf{V}) \cdot |\mathbf{G} - \mathbf{S}| \tag{12}$$

and the radius r_i along principle axis $\mathbf{B}_i'$ is accordingly increased by

$$\Delta r_i \;=\; \frac{v_i}{1 - |C\,\mathbf{B}_i' \cdot \mathbf{V}|} \tag{13}$$

Note that the typical nonperpendicularity of the major axis and the command velocity is accommodated in equation (13), allowing the projected ellipsoid to elongate along nonorthogonal projection planes.

Appendix I

Given a fixed pose $\mathbf{X}_0 \in \Re^6$, the outward normal $\mathbf{N}$ of a PC's C-surface tangent hyperplane is obtained by differentiating the PC's surface function $f(\mathbf{X})$ with respect to the 6 components of the pose and normalizing the resulting vector.

$$\bigtriangledown f \;=\; \left(\begin{array}{c} \frac{\partial f}{\partial \mathbf{X}_1} \\ \vdots \\ \frac{\partial f}{\partial \mathbf{X}_6} \end{array} \right)_{\mathbf{X}=\mathbf{X}_0} \tag{14}$$

and

$$\mathbf{N} \;=\; \frac{\bigtriangledown f}{|\bigtriangledown f|} \tag{15}$$

Taking $f(\mathbf{X_0})$ as the PC's approximate distance to $\mathbf{X}_0$, the surface tangent is approximated by the hyperplane

$$\mathbf{N} \cdot \mathbf{X} \;=\; D \tag{16}$$

where

$$D_i = \mathbf{N}_i \cdot \mathbf{X}_0 - f_i(\mathbf{X}_0) \tag{17}$$

Appendix II

A linear scaling of 6-dimensional C-space may be specified by a 6-element scaling vector $\vec{\sigma}$ and accomplished with a transformation $T : \Re^6 \rightarrow \Re^6$ which maps each point $\mathbf{X} \in \Re^6$ to $\mathbf{X}' \in \Re^6$, where $\mathbf{X}'_i = \vec{\sigma}_i \mathbf{X}_i$, $i = 1 \ldots 6$. The transformation T maps a halfspace $\{\mathbf{X} \in \Re^6 | \mathbf{N} \cdot \mathbf{X} \leq D\}$ to a new halfspace $\{\mathbf{X} \in \Re^6 | \mathbf{N}' \cdot \mathbf{X} \leq D'\}$ whose descriptors $\mathbf{N}'$ and D' are computed as follows. Let

$$\mathbf{N}^* \in \Re^6, \;\; \mathbf{N}^*_i \;=\; \frac{\mathbf{N}_i}{\vec{\sigma_i}} \;\; (i = 1 \ldots 6) \tag{18}$$

Then

$$\mathbf{N}' \;=\; \frac{\mathbf{N}^*}{|\mathbf{N}^*|} \;, \;\; D' \;=\; D\mathbf{N} \cdot \mathbf{N}' \tag{19}$$

To achieve a uniform expansion of C-space along its three rotational axes by a factor of σ_R, use scaling vector $\vec{\sigma} = [1 \; 1 \; 1 \; \sigma_r \; \sigma_r \; \sigma_r]^T$.

Alternatively, a linear scaling of 6-dimensional C-space may be specified by $n \leq 6$ scaling factors $\sigma_1 \ldots \sigma_n$ and n orthonormal axes $\mathbf{U}_1 \ldots \mathbf{U}_n$ of 6-space. We first augment the n scaling factors with $\sigma_{n+1} = \cdots = \sigma_6 = 1$ and the n axes with $6 - n$ complementary axes $\mathbf{U}_{n+1} \ldots \mathbf{U}_6$, so that $\mathbf{U}_1 \ldots \mathbf{U}_6$ form an orthonormal basis for $\Re^6$. Then transformation $T : \Re^6 \rightarrow \Re^6$ is defined

$$\mathbf{X}' = \sum_{i=1}^{6} \sigma_i \left(\mathbf{X} \cdot \mathbf{U}_i\right) \mathbf{U}_i \tag{20}$$

Halfspaces are transformed as previously, except the normal $\mathbf{N}^*$ of equation (18) is now computed as follows.

$$\mathbf{N}^* = \sum_{i=1}^{6} \frac{\mathbf{N} \cdot \mathbf{U}_i}{\sigma_i} \mathbf{U}_i \tag{21}$$

Appendix III

The contact state S formed by n primitive contacts $PC_1 \ldots PC_n$ has an associated contact space facet of dimension $6 - n$, provided that the PCs' normals $\mathbf{N}_1 \ldots \mathbf{N}_n$ are linearly independent. Given a pose $\mathbf{X} \in \Re^6$ about which to linearize contact space, the facet of S may be approximated by an $(6 - n)$-dimensional affine space, denoted by $ASpace_{\mathbf{X}}(PC_1 \ldots PC_n)$. This affine space is described by a point $\mathbf{P}$ and a vector space basis $\mathbf{V}_1 \ldots \mathbf{V}_{6-n}$ in $\Re^6$, and these descriptors may be computed as follows. For $\mathbf{P}$, choose the point associated with any contact space vertex adjacent to S (i.e., a 0-dimensional contact state whose 6 associated PCs contain $PC_1 \ldots PC_n$). Let $\mathbf{N}_1 \ldots \mathbf{N}_n$ be C-surface tangent normals for $PC_1 \ldots PC_n$, as computed in Appendix I. The vector space basis $\mathbf{V}_1 \ldots \mathbf{V}_{6-n} \perp \mathbf{N}_1 \ldots \mathbf{N}_n$ is readily computed by applying the Gram-Schmidt procedure to $\mathbf{N}_1 \ldots \mathbf{N}_n, \mathbf{U}_1 \ldots \mathbf{U}_{6-n}$, where $\mathbf{U}_1 \ldots \mathbf{U}_{6-n}$ are $6 - n$ standard axes in $\Re^6$, each independent of $\mathbf{N}_1 \ldots \mathbf{N}_n$.

Appendix IV

Given a pair of affine spaces A_1, A_2 in $\Re^6$ with respective point and basis descriptors $\mathbf{P}_1$, $\mathbf{U}_1 \ldots \mathbf{U}_{m_1}$ and $\mathbf{P}_2$, $\mathbf{V}_1 \ldots \mathbf{V}_{m_2}$, calculate the the closest point on A_1 to A_2 and the closest point on A_2 to A_1, as well as the shortest distance from A_1 to A_2, as follows. Let $\mathbf{U}_1 \ldots \mathbf{U}_{m_1}, \mathbf{U}_{m+1} \ldots \mathbf{U}_m$ be an orthonormal

basis for $span\{\mathbf{U}_1 \ldots \mathbf{U}_{m_1}, \mathbf{V}_1 \ldots \mathbf{V}_{m_2}\}$. Compute the proximity vector $\mathbf{W}$ and the distance of separation d:

$$\mathbf{R} = \mathbf{P}_2 - \mathbf{P}_1 \tag{22}$$

$$\mathbf{W}^* = \mathbf{R} - \sum_{i=1}^{m} (\mathbf{R} \cdot \mathbf{U}_i)\ \mathbf{U}_i \tag{23}$$

$$\mathbf{W} = \frac{\mathbf{W}^*}{|\mathbf{W}^*|} \tag{24}$$

$$d = \mathbf{R} \cdot \mathbf{W} \tag{25}$$

Now let $\mathbf{U}_1 \ldots \mathbf{U}_{m_1}, \mathbf{V}_1 \ldots \mathbf{V}_{m_2'}$ be a basis for $span\{\mathbf{U}_1 \ldots \mathbf{U}_{m_1}, \mathbf{V}_1 \ldots \mathbf{V}_{m_2}\}$, with $m_2' \leq m_2$. Then

$$\mathbf{P}_1 + \sum_{i=1}^{m_1} \lambda_{1i}\mathbf{U}_i + d\mathbf{W} = \mathbf{P}_2 + \sum_{i=1}^{m_2'} \lambda_{2i}\mathbf{V}_i \tag{26}$$

for some $\lambda_{11} \ldots \lambda_{1m_1}, \lambda_{21} \ldots \lambda_{2m_2'}$. The term $\mathbf{P}_1 + \sum_{i=1}^{m_1} \lambda_{1i}\mathbf{U}_i$ is the closest point on A_1 to A_2, and the term $\mathbf{P}_2 + \sum_{i=1}^{m_2'} \lambda_{2i}\mathbf{V}_i$ is the closest point on A_2 to A_1. (26) is a consistent system of 6 equations in $m_1 + m_2' \leq 6$ unknowns, and its solution parameterizes the closest points on the two affine spaces.

Appendix V

Given an ellipsoid whose principle axes correspond to the standard axes of n-space:

$$\sum_{i=1}^{6} D_i X_i^2 = 1 \tag{27}$$

it is easy to show that the point $\mathbf{X}$ on the ellipsoid's surface that corresponds to the direction $\mathbf{U}$ is just $\lambda_{\mathbf{U}}\mathbf{U}$ where

$$\lambda_{\mathbf{u}} = \frac{1}{\sqrt{\sum_{i=1}^{6} D_i U_i^2}} \tag{28}$$

5 Implementation and Discussion

The fine-motion planning technique described above was implemented in Pop-11, Prolog, and C running on a Sun-4 workstation. The planner has produced trajectories for a square peg-in-hole assembly (e.g. see figure 3). The refinement process is rapid, producing executable trajectories in a second or less. Peg motions specified by the planner have been performed by a Zebra-Zero robot. The robot operates in position-servo mode to execute command displacements between goal points in contact space, as well as to displace along the contact normals in order to achieve nominally specified bias forces. A visual servoing facility has also been employed to correct positioning errors at each goal pose. Future work will explore the on-line acquisition of compliances through associative reinforcement learning.

6 Conclusion

A methodology for synthesizing fine-motion plans in the contact space of narrow-clearance assemblies was presented. Supplied with a nominal trajectory computed *a priori*, fine-motion planning proceeds within the local contact spaces surrounding problematic trajectory sites where the assembly may fail. The local contact space surrounding each critical point is searched for a traversable sequence of contact states, and a command trajectory is synthesized for traversing the selected states. Our technique has produced trajectories for a square peg-in-hole assembly which have been executed successfully by a Zebra-0 robot.

7 References

1. Buckley, C.E. (1985), "A proximity metric for continuum path planning", *9th International Joint Conference on Artificial Intelligence*, pp. 1096-1102.
2. Caine, M.E., Lozano-Pérez, T., Seering, W.P. (1989), "Assembly strategies for chamferless parts", *Proc. IEEE International Conference on Robotics and Automation*, pp. 472-477.
3. Canny, J.F. (1989), "On computability of fine motion plans", *Proceedings of the IEEE International Conference on Robotics and Automation*, Vol. 1, pp. 177-182.

4. Dakin, G., Popplestone, R.J. (1993), "Contact space analysis for narrow-clearance assemblies", *Proc. IEEE International Symposium on Intelligent Control*, pp. 542-7, and Technical Report 93-59, C.S. Dept., Univ. of Massachusetts, Amherst MA.
5. Dakin, G., Popplestone, R.J. (1993), "Fine-motion planning in the contact space of narrow-clearance assemblies", *Proceedings of the IASTED International Conference on Robotics and Manufacturing*, pp. 206-8, and Technical Report 93-60, C.S. Dept., Univ. of Massachusetts, Amherst MA.
6. Dakin, G., Popplestone, R.J. (1992), "Simplified Fine-Motion Planning in Generalized Contact Space", *Proceedings of the IEEE International Symposium on Intelligent Control*, pp. 281-6.
7. Donald, B.R. (1984), "Motion planning with six degrees of freedom", Technical Report AI-TR-791, A.I. Laboratory, MIT.
8. Erdmann, M. (1984), "On motion planning with uncertainty", Tech. Report AI-TR-810, A.I. Laboratory, MIT.
9. Koutsou, A. (1986), "Parts mating by moving objects in contact", PhD Thesis, Dept. of A.I., Edinburgh University.
10. Laugier, C. (1989), "Planning fine motion stategies by reasoning in contact space", *Proceedings of the IEEE International Conference on Robotics and Automation*, pp.653-659.
11. Liu, Y. (1990), "Symmetry groups in robotic assembly planning", PhD Dissertation, COINS Dept., U.Mass., Amherst MA.
12. Lozano-Pérez, T., Mason, M., Taylor, R.H. (1984), "Automatic synthesis of fine-motion strategies for robots", *International Journal of Robotics Research*, Vol. 3, No. 1, pp. 3-24.
13. Peshkin, M.A. (1990), "Programmed compliance for error corrective assembly", *IEEE Transactions on Robotics and Automation*, Vol 6, No. 4, pp. 473-482.
14. Popplestone, Ambler, A.P., Bellos, I. (1980), "An interpreter for a language describing assemblies", Artificial Intelligence, Vol. 14, No. 1, pp. 79-107.
15. Salisbury, J.K. (1980), "Active stiffness control of a manipulator in Cartesian coordinates", *Proceedings of the 19th IEEE Conference on Decision and Control*, pp. 95-100.
16. Whitney, D.E. (1982), "Quasi-static assembly of compliantly supported rigid parts", *Journal of Dynamic Systems, Measurement, and Control*, Vol. 104, pp. 64-77.